Progress In Electromagnetics Research C, Vol. 92, 201–213, 2019

High-Precision Phase Shifting and Real-Time Calibration of Phased Arrays for Passive Millimeter-Wave Imaging Applications

Canwei Xin*, Anyong Hu, Kai Liu, Wenjie Lv, and Jungang Miao

Abstract—The design and calibration of high-precision analog phase shifters are crucial issues for phased arrays interferometric passive millimeter-wave imaging systems. In this paper, a high-precision analog phase shifter is presented for phased arrays interferometric passive millimeter-wave security sensing applications, which realizes analog phase shifting function by controlling high-precision DAC (digital to analog conversion) with FPGA. It is known that pre-measured phase delay of a phased array channel is a prerequisite for beam pointing control. However, since many active devices are included in phased array channel link, the phase delay would be affected by various factors such as device moving and ambient temperature. So, high-precision phase shifting of phased arrays could be achieved only by measuring and calibrating phases when all components of the system are under normal working conditions. The algorithm proposed in this paper makes it possible to measure and calibrate phases when all sub-modules are integrated into the system, and each component is under normal working state, thus effectively avoiding the errors caused by environmental changes when the laboratory-measured results are put into practical use. Meanwhile, the algorithm is tested on Ka-band phased arrays interferometric passive millimeter-wave imaging system. It turns out that the phase accuracy of phased array channel can reach $5^\circ \pm 1.5^\circ$, and it only takes 2 minutes to complete the phase calibration of 256 arrays.

1. INTRODUCTION

Interferometric imaging is a well-known technique for earth remote sensing [1, 2] and radio astronomy [3, 4] and has received increasing attention in security sensing applications, such as concealed-weapons and explosives detection [5–9]. The basic element of an interferometric imaging system is a two-element interferometric correlation radiometer [9] which consists of two receiver chains (an antenna and a receiver) and a cross-correlator. In order to improve the imaging resolution, aperture synthesis using interferometric technique has been successfully used for synthesizing very large apertures for radio telescopes like Very Large Array (VLA), Atacama Large Millimeter/sub-millimeter Array (ALMA), and Allen Telescope Array (ATA) [10]. Two versions of synthetic aperture passive millimeter wave imagers for security screening application, i.e., BHU-2D [11] and BHU-2D-U [12], have already been developed and tested by Beihang University. BHU-2D has 24 receiving elements with 160 MHz bandwidth, and BHU-2D-U has 48 receiving elements with 200 MHz bandwidth [13]. The work presented in this article is a part of further enhancements in this system targeted to improve sensitivity and increase resolution in video rate imaging. The new imaging system will use an increasing number of antennas to achieve these objectives, i.e., approximately 256, with bandwidth greater than 4 GHz in W band. Considering the amount of processing required for a 2-D aperture synthesis imager in the context of current state of the art digital technology, it is almost not able to use the digital cross-correlator. Analog cross-correlator featured with fast calculation and wide bandwidth features is the best choice.

If layout design of all the 256 receiving elements adopts aperture synthesis imaging mechanism, it needs $256 \times 256 = 65536$ cross-correlators and 256 1-To-256 power dividers, in which case the number

Received 22 February 2019, Accepted 30 April 2019, Scheduled 15 May 2019
* Corresponding author: Canwei Xin (280168676@qq.com).
The authors are with the School of Electronics and Information Engineering, Beihang University, Beijing 100191, China.

is too large to be easily integrated into the system. Therefore, horizontal layout design adopts phased array, and vertical layout design adopts aperture synthesis. As a result, the number of cross-correlators and the 1/16 power dividers can be reduced to $16 \times 16 = 256$ and 16, respectively, and the design and calibration of the high-precision phase shifter are crucial issues for phased arrays interferometric imaging systems.

Phased array channel is usually composed of a receiving antenna, a low noise amplifier, a mixer, a phase shifting module, a power distribution network, RF cables, etc. High-precision phase shifter, usually analog phase shifter, is one of the core modules, whose output phase is controlled by the output voltage subdivided by high-precision DAC chip. Among these modules are many active devices, whose phase delays vary with device moving and the change of ambient temperature. Two main factors of phase changes are: 1) variations of high-precision phase shifter's amplitude and phase control parameters; 2) changes in network parameters of other components.

Control parameters of a high-precision phase shifter are usually measured by vector network analyzer under laboratory conditions. High-precision DAC outputs subdivided step voltage under the regulation of logic control, after which vector network analyzer measures S_{21} parameters of phase shifter at each step voltage, thus obtaining the mapping relationship between DAC control voltage and phase shifter's amplitude and phase parameters. Given that DAC control circuit and phase shifter are both active devices, their port network parameters vary with device moving and the change of temperature. Since phase-shifting network demands high precision, the errors caused by this cannot be ignored. Laboratory testing methods and data processing methods have been presented in [14, 15]. However, the effects of environmental changes mentioned above are not taken into consideration.

Phased array's phase-shifting accuracy is mainly affected by the initial phase measurement accuracy for phased array channels and the stability of its phase. Phase information of phased array channel varies with the change of temperature or changes with the replacement of RF cables. In other words, the calibration results of initial phase cannot stay accurate and effective for a long time, so the initial phase calibration is required. The job usually has to be done in a microwave anechoic chamber by means of vector network analyzer. This process is so difficult, time-consuming, and environmentally demanding that it cannot even be realized under certain application conditions. As a result, we have no choice but replace the whole system, which is equally time-consuming and costly. In [16], a solution to this problem is proposed. However, it lacks specific algorithm implementation and validation of experimental data. Only temperature's effect on system phase is taken into account. In multicomponent module, this solution cannot be adopted when it is impossible to measure the temperature precisely. Novel measurement and calibration methods for phased array antennas, such as Near-field scanning method [17–19], REV (Rotating Electricity Vector) method [20–24], phased-shift measurement method [25], and mutual coupling measurement method [26], have been studied in recent years, all of which provide specific implementation procedures and experimental or simulative verification. However, without analysis of the system phase which varies with device moving, ambient temperature changes and corresponding solutions, real-time phase calibration still cannot be achieved [27, 28].

In this paper, a high-precision online phase calibration method for phased array channels is proposed. It can not only solve the problem that port network parameters of phase shifter itself and other components vary with device moving, ambient temperature changes, and other factors but also achieve quick real-time calibration of phased arrays. This paper first analyses the temperature-drift characteristic of phase and then illustrates the real-time measurement of amplitude and phase parameters. The real-time phase calibration method of phased array channel is discussed in the third part. Finally, experimental verification and error analysis are made on interferometric passive millimeter-wave imaging system.

2. DESIGN AND ERROR ANALYSIS OF HIGH-PRECISION PHASE SHIFTER MODULE

Phase shifters are divided into digital phase shifters and analog phase shifters. The former can be directly linked up to a digital system, and it is easy to control the whole process. Its disadvantage is that the phases which can be shifted are discrete and small in number, so the accuracy cannot be

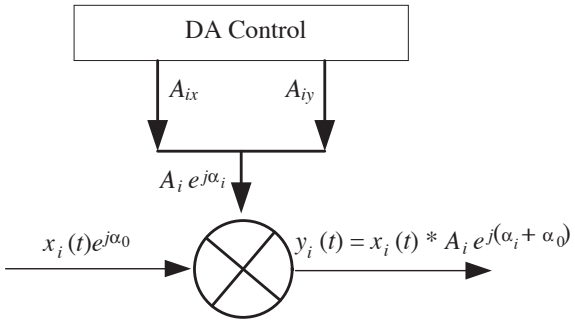

Figure 1. Principle of high-precision analog phase shifter.

guaranteed. The latter is often used in systems requiring high-precision phase shifting, whose output phase is controlled by the input voltage. Theoretically, continuous voltage inputs generate continuous adjustable phase outputs, thus achieving 360° phase modulation without errors. The disadvantage of an analog phase shifter is that it cannot be directly connected to a digital control system. In order to realize digital phase shifting, bridge connection with the aid of DAC devices is necessary. As shown in Figure 1, the accuracy of an analog phase shifter is converted to the voltage control accuracy of DAC.

2.1. Design Principle of High-Precision Phase Shifter Module

The design block diagram of high accuracy phase shifter module is given in Figure 2. The RF signal propagates from port 1 to port 2, which is first split into in-phase (I) and quadrature (Q) components. The variable attenuators independently scale I and Q components of the RF input. The attenuator outputs are then summed and buffered to the output.

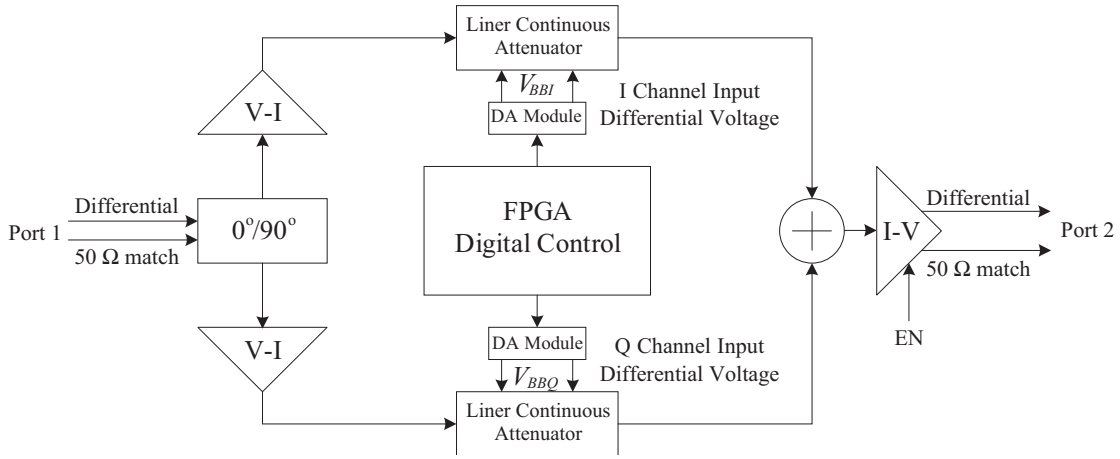

Figure 2. High-precision phase shifter module architecture.

By using FPGA to control the relative amounts of I and Q components that are summed, continuous magnitude and phase control of the gain is possible. Consider the vector gain representation of the AD8341 expressed in polar form in Figure 3. The attenuation factors for I and Q signal components are represented on the x- and y-axes, respectively, by the baseband inputs, V_{BBI} and V_{BBQ}. The resultant of their vector sum represents the vector gain $\vec{A}$, which can also be expressed as a magnitude $|A|$ and phase θ [16].

The outermost circle represents the maximum gain magnitude of unity. The circle origin implies, in theory, a gain of 0. In practice, circuit mismatches and unavoidable signal feed through limiting the minimum gain to approximately -34.5 dB. The phase angle between the resultant gain vector and the positive x-axis is defined as phase shift.

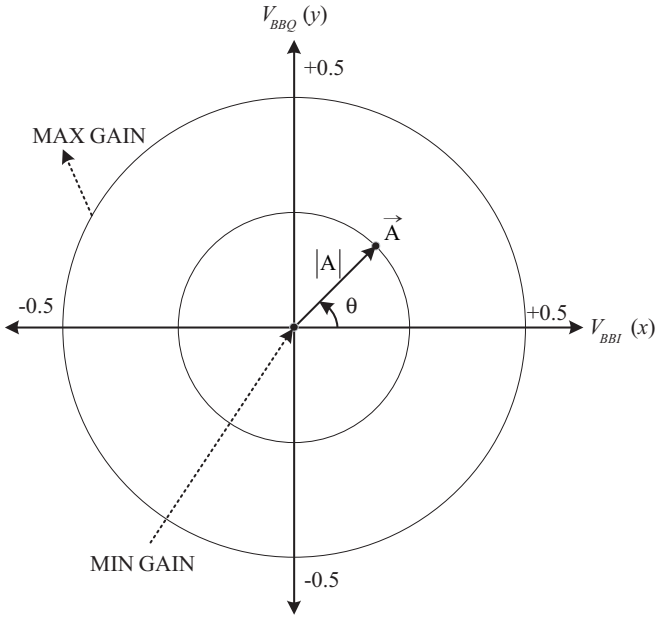

Figure 3. Modulation vector diagram.

The correspondence between the desired gain and phase set points, Gain_{SP} and Phase_{SP}, and the Cartesian inputs, V_{BBI} and V_{BBQ}, is given by simple trigonometric identities

$$\text{Gain}_{SP} = \sqrt{(V_{BBI}/V_O)^2 + (V_{BBQ}/V_O)^2} \tag{1}$$

$$\text{Phase}_{SP} = \arctan(V_{BBQ}/V_{BBI}) \tag{2}$$

where:

V_O is the baseband scaling constant.

V_{BBI} and V_{BBQ} are the differential I and Q baseband voltages, respectively.

2.2. Design of High-Precision Phase Shifter Module

The vector modulator of the analog phase shifter module adopts AD8341 chip [29]. The frequency range of RF channel is 1.5 GHz $\sim$ 2.4 GHz; the adjustable range of continuous amplitude is -4.5 dB $\sim$ 34.5 dB; the adjustable range of continuous phase is $0^\circ \sim 360^\circ$; and that of voltage is -0.5 V $\sim$ 0.5 V. AD5668 chip is utilized in DAC control module [30]. This kind of chip is an 8-channel, 16-bit DAC whose effective bit is 13 bits, and external reference voltage is 1.2 V. The EP3C25Q240 model of Altera is used in FPGA digital control module [31], and the entity of the high-precision phase shifting module is shown in Figure 4.

The DAC contains 8 channels, and the precision is 16 bits, of which only 13 bits are effective. Also, the external reference voltage of the chip is 1.2 V, and the minimum step voltage is $1200\,\text{mV}/2^{13} = 0.1465\,\text{mV}$. The voltage regulation range of vector modulator is 1 V, and the adjustable range of phase is 360°, then the adjustable phase of unit voltage is $1000\,\text{mV}/360^\circ = 2.78\,\text{mV/deg}$. Phase shifter module's theoretical adjustable precision is as follows.

$$\frac{0.1465\,\text{mV}}{2.78\,\text{mV/deg}} = 0.0527\ \text{deg} \tag{3}$$

After the hardware design of phase shifter module is completed, it is necessary to measure S_{21} of phase-shifting channel to establish a one-to-one mapping relationship between digital logic control voltage and phase shifter. In the laboratory, vector network analyzer can be used to directly measure S_{21} of phase shifter's phase-shifting channel, whose test block diagram is shown in Figure 5. The RF

Figure 4. 8-channel phase shifter module.

input and output ports of phase shifter module are connected to the two ports of the vector network analyzer, and FPGA module is connected to the computer through SPI interface.

First, DAC voltage configuration is figured out by the computer, and then the data are transmitted to FPGA module through SPI bus. FPGA module sends the received control instruction to DAC, and then DAC module configures the required voltage to vector modulator. Finally, vector network analyzer measures S_{21} and sends the data to the computer. Thus, one voltage-to-phase mapping point measurement is completed. The two-dimensional plane voltage-to-phase mapping point sparse test in Figure 3 is completed by repeating this process.

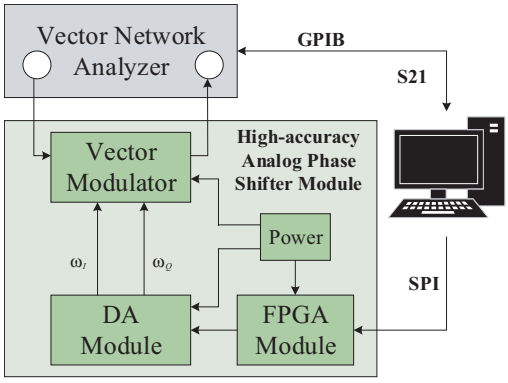

Figure 5. Test block diagram of phase shifter module S_{21}.

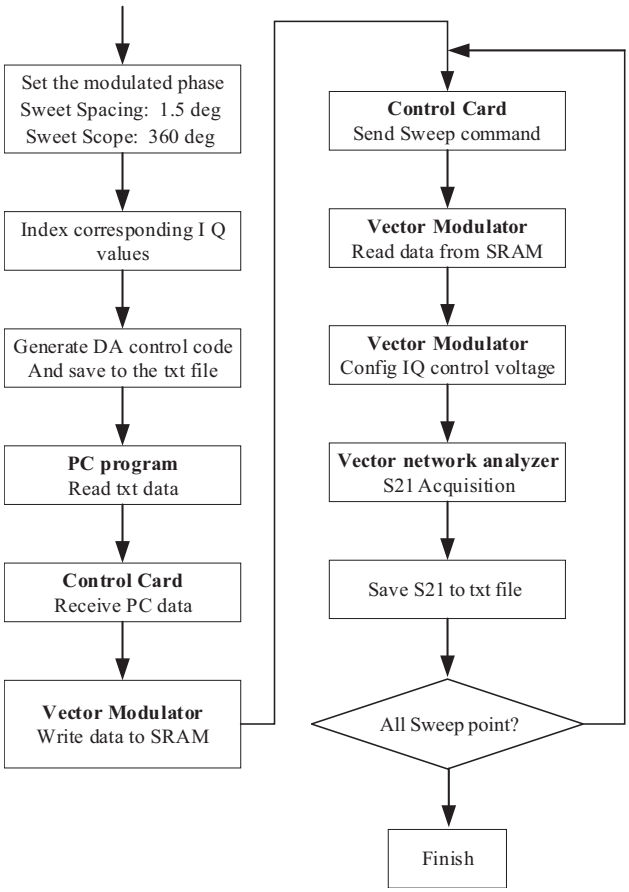

Figure 6. Phase modulation accuracy test of the phase shifter module.

After that, the phase-to-phase test and verification is carried out by using the testing method of Figure 5. The required phase is calculated by computer first and then scented to the high-precision phase shifter module. Then the modulated phase is measured by a vector network analyzer. The test flowchart is shown in Figure 6.

The test results are shown in Figure 7. The configuration phase range is $0° \sim 360°$, and the step is $1.5°$ with 240 points. The phase standard deviation is $0.029°$, and the amplitude standard deviation is 0.043 dB. The amplitude and phase index reach the theoretical accuracy of calculation in Formula (3), which shows that the hardware design meets the design requirements.

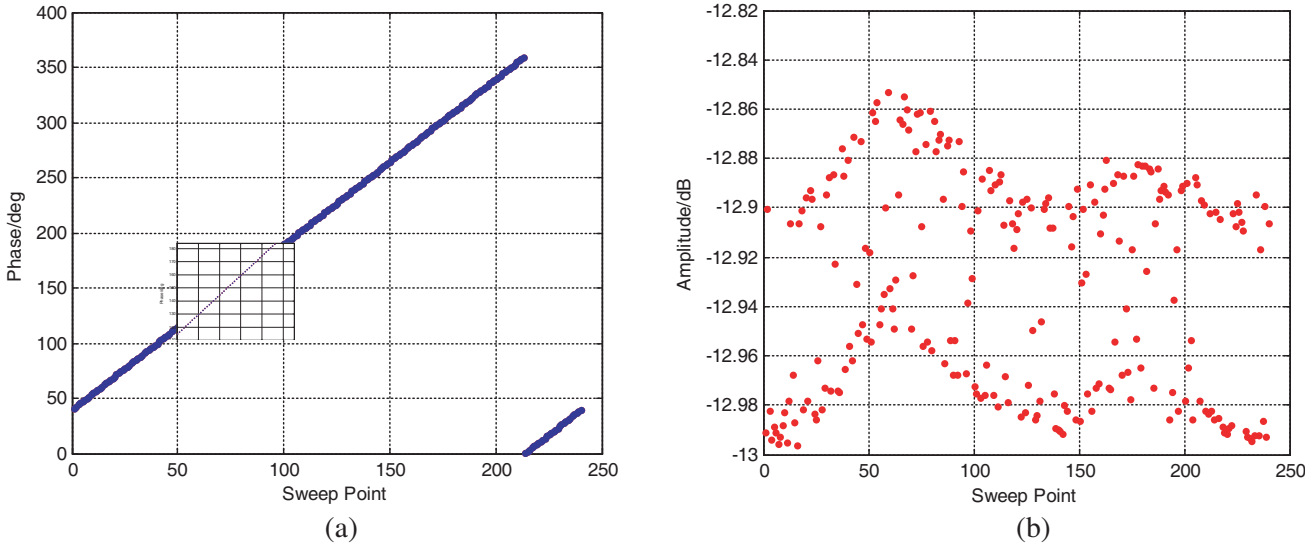

(a) (b)

Figure 7. (a) Phase modulation accuracy of phase shifter module. (b) Amplitude modulation accuracy of phase shifter module.

2.3. Error Analysis of High-Precision Phase Shifter Module

The test in Figure 7 was completed in a very short time, and the test verification platform did not experience any changes. However, in the practical use of high-precision phase shifter, it needs to be integrated into a system; therefore, moving the shifter and dissembling the cables are unavoidable. Besides, the actual ambient temperature and laboratory testing temperature cannot be completely consistent, and long-term use will also lead to device aging and other issues. In order to study the effects of environmental factors on the phase-measurement accuracy, the testing scheme in Figure 5 is adopted to carry out repetitive connection test and conduct tests with changing system voltage and ambient temperature. The test results are shown in Figure 8. Each group of test samples has more

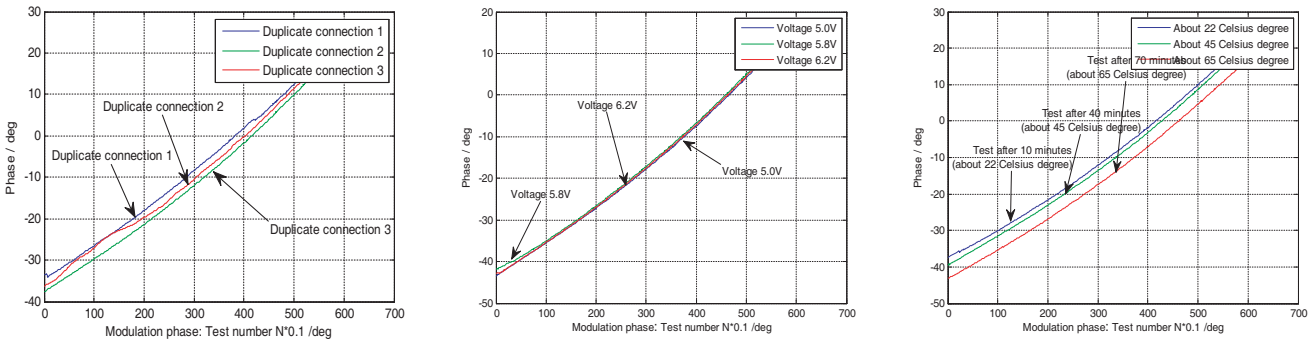

(a) (b) (c)

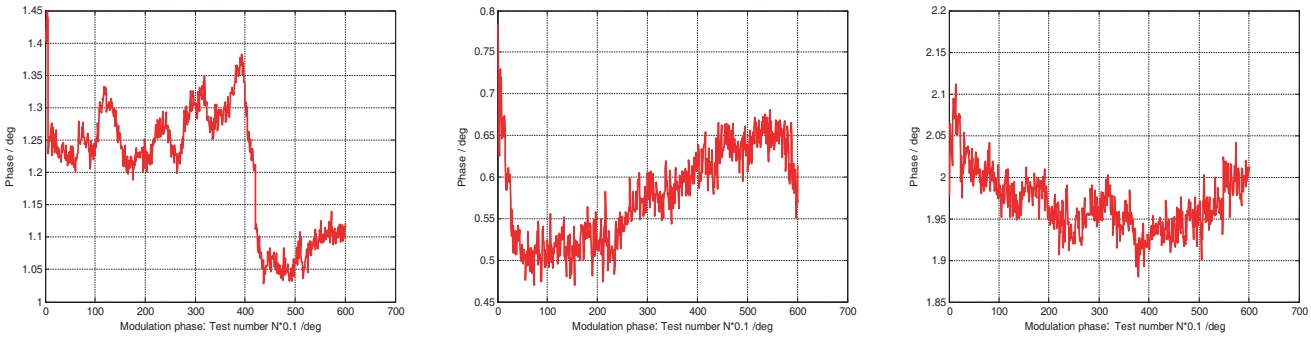

(d) (e) (f)

Figure 8. (a) Effect of repeated connection on phase curve. (b) Standard deviation of repeated connection on phase curve. (c) Effect of voltage on phase curve. (d) Standard deviation of voltage on phase curve. (e) Effect of temperature on phase curve. (f) Standard deviation of temperature on phase curve.

than ten times. In order to analyze the problem more clearly, only three curves are displayed, but the statistical standard deviation curve uses all the sample data.

From the test results, it can be seen that the phase curves are not completely coincident, and the degree of non-coincidence is represented by statistical standard deviation. The influence of repetitive connection and voltage on phase curve is about 1.2° and 0.7°, respectively. Ambient temperature's influence is measured by the length of test interval, and it is about 2.1°. For high-precision phase shifter, the measurement error of 2° in system integration is unacceptable, while the laboratory testing scheme in Figure 5 is not suitable for the complex high-precision phase shifting system. Then a real-time on-line measurement calibration method is proposed, which can help overcome the limitations of the testing method in Figure 5.

3. S_{21} ONLINE MEASUREMENT OF PHASE SHIFTER MODULE

As shown in Figure 9, the high-precision phase shifter module is integrated into the latest Interferometric Passive Millimeter-Wave Imaging System, which has already been developed and tested by Beihang University. The imaging system includes an array antenna, a low noise amplifier, a mixer module, a phase shifter module, a power divider, a correlator module, and a data acquisition and processing system.

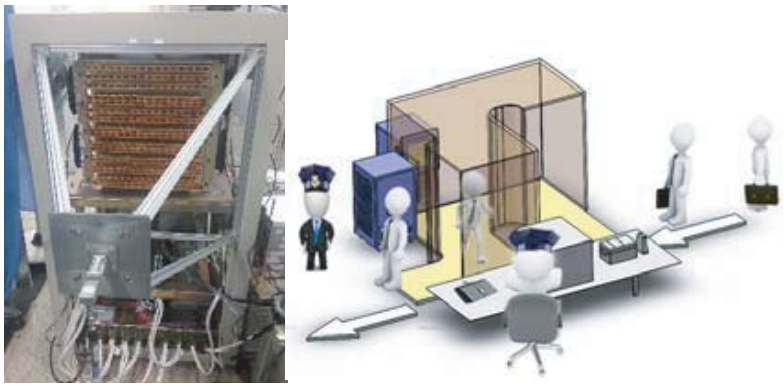

(a) (b)

Figure 9. (a) The device of interferometric passive millimeter-wave imaging system. (b) The demonstration interferometric passive millimeter-wave imaging system.

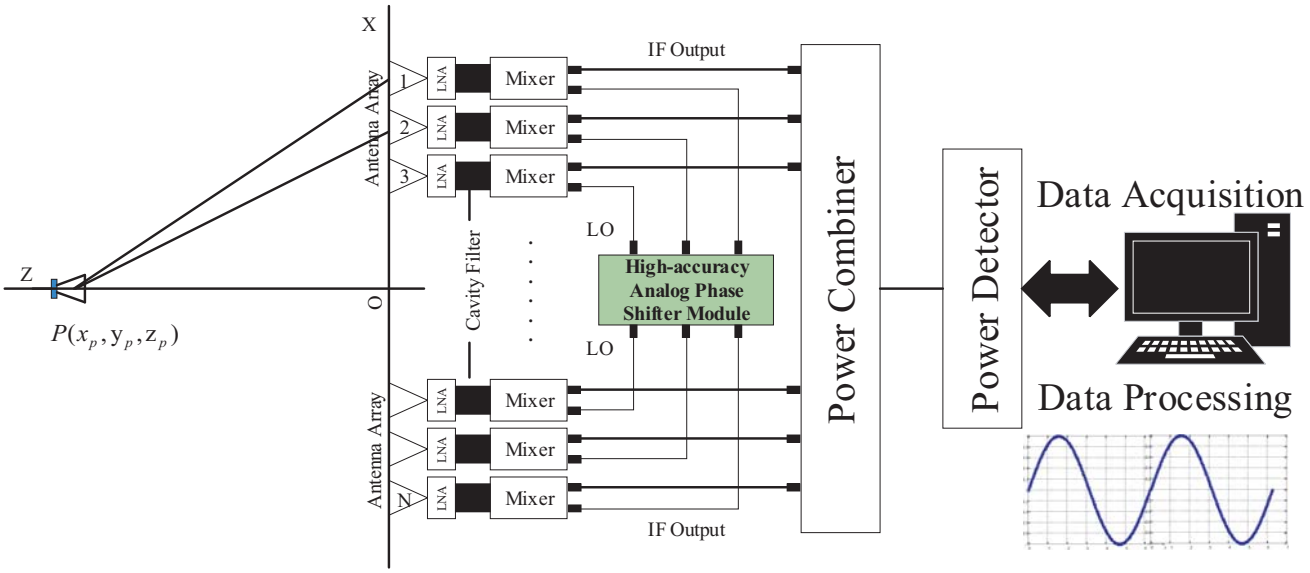

Figure 10. The diagram of interferometric passive millimeter-wave imaging system.

The high-precision analog phase shifter module is connected to a local oscillator branch of the mixer, as shown in Figure 10, and a noise source is placed at P point in the geometric center of the array. The phase of the received signal is changed by adjusting the local oscillator phase of the mixer. The frequency of the local oscillator signal is 2 GHz, and the frequency of the mixer signal is 32 GHz. So, phase modulator coefficient of the phase shifter is 16.

Suppose that channel 1 and channel 2 receive signals S_1 and S_2 from the noise source placed at point P, which can be expressed as:

$$S_1 = A_1 e^{j(\omega t+\theta_1)} = A_1\cos(\omega t+\theta_1) + jA_1\sin(\omega t+\theta_1) \tag{4}$$

$$S_2 = A_2 e^{j(\omega t+\theta_2)} = A_2\cos(\omega t+\theta_2) + jA_2\sin(\omega t+\theta_2) \tag{5}$$

where A_1 and A_2 represent the amplitudes of S_1 and S_2, respectively; θ_1 and θ_2 represent the initial phases of S_1 and S_2; ω represents the angular frequency of S_1 and S_2. After the two signals are handled by power combiner and power divider, the following equation can be obtained.

$$R_{\text{sum}} = A_1\cos(\omega t+\theta_1) + A_2\cos(\omega t+\theta_2+\Delta) \tag{6}$$

where Δ is the incremental phase corresponding to the incremental voltage attached to channel 2. When the signals pass through square-rate detection and low-pass filter, the following result is obtained.

$$|R_{\text{sum}}|^2 = K\left[\frac{A_1^2}{2} + \frac{A_2^2}{2} + A_1A_2\cos(\theta_1-\theta_2-\Delta)\right] \tag{7}$$

K denotes the square-rate detection sensitivity, and its value is constant. From Equation (7) it is inferred that when $\Delta = \theta_1 - \theta_2$, $|R_{\text{sum}}|^2$ gets the maximum. A set of $|R_{\text{sum}}|^2$'s values can be obtained by controlling Δ's ergodic value from 0° to 360°. Deal with these values with the method of curve fitting and calibrate one cycle's 90° at the maximum point $|R_{\text{sum}}|^2_{\max}$, then the one-to-one mapping relation between incremental voltage and phase can be obtained.

The function is verified on the Interferometric Passive Millimeter-Wave Imaging System in Figure 9. Select array channel 1 in Figure 10 as the reference channel, to which phase shifter configures a fixed voltage, and fix its channel phase on a specific phase; then conduct S_{21} test on array channel N and scan its voltage with phase shifter. The scanning voltage is $\left|\vec{A}\right| e^{j\varphi}$ ($\varphi = 1°, 2°, ..., 360°$). $\vec{A}$ expresses the radius of scanning voltage, and the scanning interval is 1°. Sampling rate is 30 kbps while the residence time for each scanning phase is 1 ms, so each point is the statistical average of 30 samples. Figure 11(a)

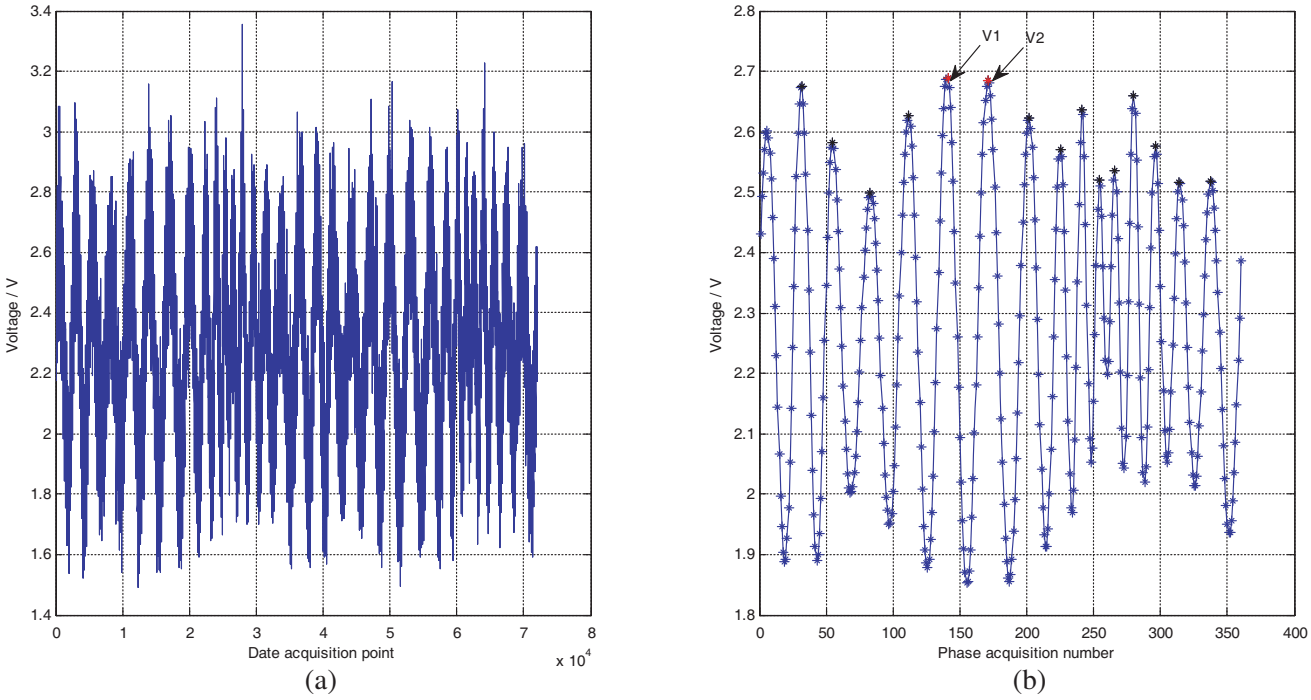

Figure 11. (a) Test data of online system S_{21} sparse measurement. (b) Statistical average data of online system S_{21} sparse measurement.

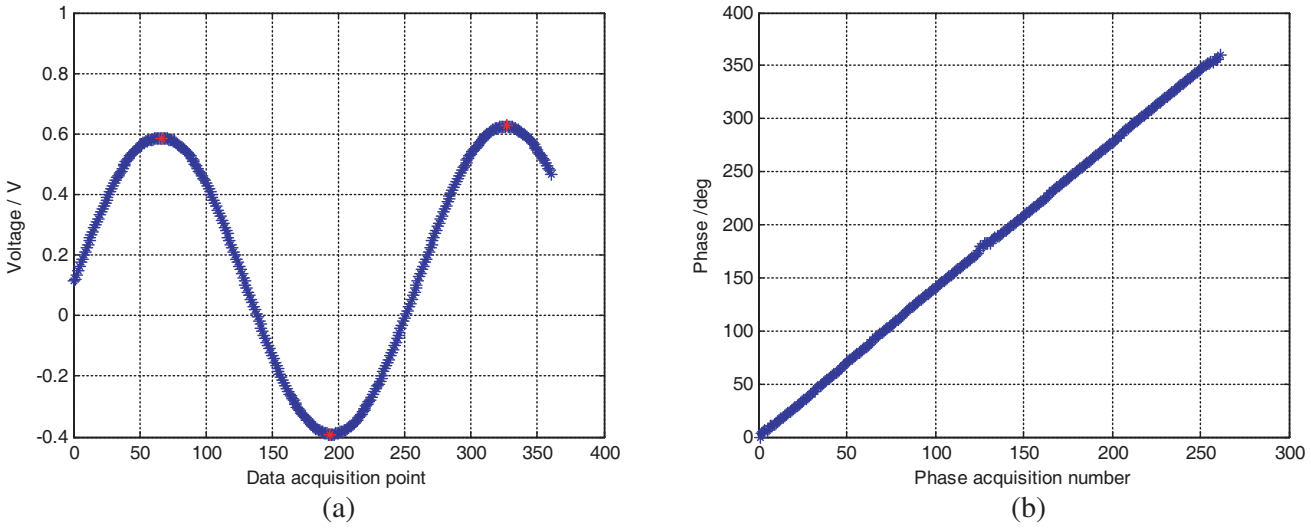

Figure 12. (a) Output voltage of detector. (b) Phase curve of the test data.

shows the test data of online system S_{21} sparse measurement, and Figure 11(b) shows the statistical average data.

Next, intensive testing is conducted. Select a circle $(V1, V2)$ with the most stable peak changes from the 16 circles in Figure 11(b), index the phase's starting and ending points (φ_a, φ_b), and then conduct voltage sweep for array channel N. The scanning voltage is expressed as $\left|\vec{A}\right| e^{j\varphi}$ $(\varphi = \varphi_a + 1/360, \varphi_a + 2/360, ..., \varphi_b)$. Figure 12 shows the result of this test: (a) demonstrates the raw data of intensive testing, and (b) is obtained by intercepting a full cycle expansion. Finally, the high-precision mapping relation between voltage and phase is acquired.

4. ONLINE PHASE CALIBRATION OF PHASED ARRAY CHANNELS

The principle of online phase calibration of phased array channel is shown in Figure 13, and the high-precision phase shifter module can achieve 0°–360° phase modulation.

Channel 1 Calibration: High-precision phase shifter module controls phased array channel 1 and increases the phase from 0° to 360° in turn. When channel 1 rotates in a 360° range, other channels are fixed at a specific unknown phase. On each rotation phase, the combined power values of 16 channels are calculated, and then the initial phase, i.e., residual error, is calculated by adopting the curve fitting algorithm.

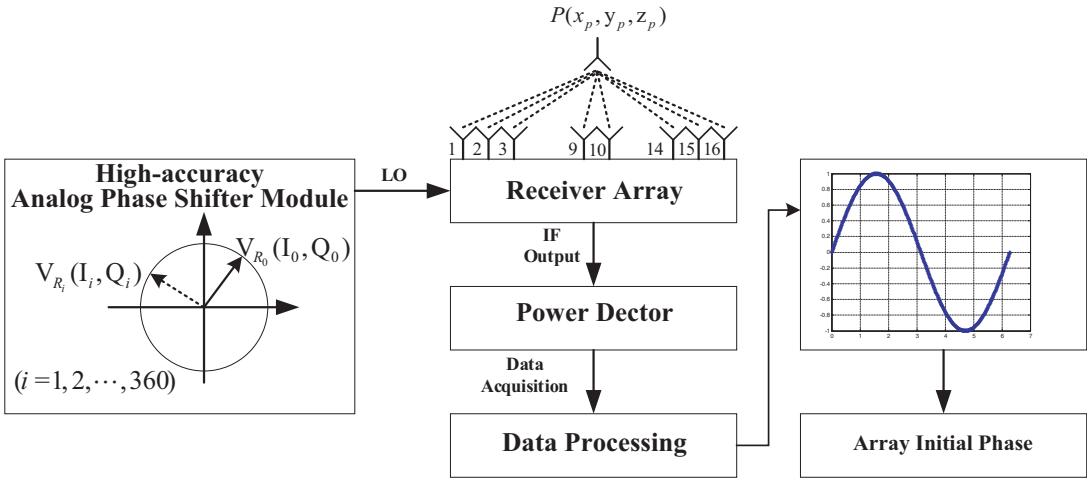

Figure 13. Functional block diagram of high-speed phase calibration.

Table 1. Channel phase residual measurement of 16 × 16 phased array.

Array Number	Residual phase after Iteration times N				
	iteration 0 (deg)	iteration 1 (deg)	iteration 2 (deg)	iteration 3 (deg)	iteration 4 (deg)
A1	37.8	12.8	17	14	5
A2	114	82.6	96.4	18.3	3.6
A3	28.7	17.2	7.5	2.5	3.4
A4	26.4	11.2	4	2.7	2.7
A5	73.3	30.4	13.9	8.3	6.1
A6	86.2	25.2	8.2	15.9	10
A7	102	32.2	11.5	11.6	6.3
A8	53.7	18.3	20.3	7.1	3.8
A9	113	115	23.8	5.1	4.4
A10	108	43.2	4.7	4.6	2.5
A11	44.1	12.4	7.1	4.5	11
A12	21.4	26.2	32.9	8.4	3.4
A13	17.6	16.7	2.9	3.1	3.2
A14	38.3	13.6	3.6	9.7	7.7
A15	48.3	33	20.6	6.4	3.5
A16	109	36	14.5	15.8	13

Channel 2 Calibration: High-precision phase shifter module controls phased array channel 2 and increases the phase from 0° to 360° in turn. When channel 2 rotates in a 360° range, other channels are fixed at a specific unknown phase. On each rotation phase, the combined power values of 16 channels are calculated, and then the initial phase, i.e., residual error, is calculated by adopting the curve fitting algorithm.

Similarly, 16 channels are calibrated. In this way, once iteration calibration of all the phased array channel phase is completed, the second, third, ..., nth ones can be carried out in turn until the phase residual error meets the requirements of the system.

Table 1 shows four times iteration calibration in the Interferometric Passive Millimeter-Wave Imaging System of Figure 8, after which the standard deviations of channel phase residual errors of each array are mostly about 5°. This 5° is the phase shifting accuracy of the RF end. Equivalent accuracy of the phase shifter is $5°/16 = 0.3125°$.

The horizontal and vertical directions of millimeter wave radiometer antenna are called phased array direction and synthetic aperture direction respectively. Since the arrays (A1, A2, ..., A16) of the phased array are independent from each other, all phased array channels calibration in the synthetic aperture direction can be achieved simultaneously when calibrating the phased array direction. The integral time of the detector is calculated by 10 ms. When the phase is calibrated, the total time of each phase point is 10 ms. It takes about 60 s to complete 360 phase points of all 16 channels of the array. At the same time, the collected data of power detector are saved in the computer. The channel phase can be calculated by adopting the curve fitting algorithm, and then it takes about 1.5 minutes to configure the residual phase by vector modulator. So, one iteration calibration of all the phased array channels can be completed in 2 minutes.

5. CONCLUSIONS

High-precision phase shifting and real-time calibration of phased arrays make it possible for passive millimeter wave imaging system to be uninterrupted working, which improve the stability and performance of the imaging system. The algorithm proposed in this paper achieves measurement and calibration of the phased array channel phases when all sub-modules are integrated into the system, and each component is preheated to the normal working condition. It effectively avoids the phased array channel phases errors of measurement and calibration caused by environmental changes when laboratory-measured results are put into practical use. The phase parameters of phase shifter module are measured sparsely first and then intensively. Finally, the actual validation of the equivalent phase accuracy is 0.3125°. The real-time phase calibration of phased array channel is verified in the Interferometric Passive Millimeter-Wave Imaging System. After four times iteration calibration, the standard deviation of the phased array channel phase residual is mostly about 5°, and one iteration calibration of all the phased array channels can be completed in 2 minutes, which can be applied to systems requiring real-time and fast phase calibration.

ACKNOWLEDGMENT

This work was supported by the National Key Research and Development Program of China, grant number 2016YFC0800400, and by the National Natural Science Foundation of China, grant number 61731001.

REFERENCES

1. Le Vine, D. M., "The sensitivity of synthetic aperture radiometers for remote sensing applications from space," *Radio Sci.*, Vol. 25, 441–453, 1990.
2. Le Vine, D. M., "Synthetic aperture radiometer systems," *IEEE Trans. Microw. Theory Tech.*, Vol. 47, 2228–2236, 1999.
3. Weber, J. C. and M. W. Pospieszalski, "Microwave instrumentation for radio astronomy," *IEEE Trans. Microw. Theory Tech.*, Vol. 50, 986–995, 2002.

4. Thompson, A. R., J. M. Moran, and G. W. Swenson, Jr., *Interferometry and Synthesis in Radio Astronomy*, Wiley, New York, NY, USA, 2001.
5. Yujiri, L., M. Shoucri, and P. Moffa, "Passive millimeter wave imaging," *IEEE Microw. Mag.*, Vol. 4, 39–50, 2003.
6. Appleby, R. and H. B. Wallace, "Standoff detection of weapons and contraband in the 100 GHz to 1 THz region," *IEEE Trans. Antennas Propag.*, Vol. 55, 2944–2956, 2007.
7. Ahmed, S. S., A. Schiessl, F. Gumbmann, M. Tiebout, S. Methfessel, and L. P. Schmidt, "Advanced microwave imaging," *IEEE Microw. Mag.*, Vol. 13, 26–43, 2012.
8. Patel, V. M., J. N. Mait, D. W. Prather, and A. S. Hedden, "Computational millimeter wave imaging: Problems, progress and prospects," *IEEE Signal Process. Mag.*, Vol. 33, 109–118, 2016.
9. Nanzer, J. A., *Microwave and Millimeter-wave Remote Sensing for Security Applications*, Artech House, Norwood, MA, USA, 2012.
10. Wang, C., X. Xin, B. Liang, et al., "Quadrature errors and DC offsets calibration of analog complex cross-correlator for interferometric passive millimeter-wave imaging applications," *Sensors*, Vol. 18, 677, 2018.
11. Zheng, C., X. Yao, A. Hu, and J. Miao, "A passive millimeter-wave imager used for concealed weapon detection," *Progress In Electromagnetics Research B*, Vol. 46, 379–397, 2013.
12. Zheng, C., X. Yao, A. Hu, and J. Miao, "Initial results of a passive millimeter-wave imager used for concealed weapon detection Bhu-2d-U," *Progress In Electromagnetics Research C*, Vol. 43, 151–163, 2013.
13. Asif, M., X. Guo, J. Zhang, et al., "Frequency based design partitioning to achieve higher throughput in digital cross correlator for aperture synthesis passive MMW imager," *Sensors*, Vol. 18, 1238, 2018.
14. Li, J., "The measure and the application of the vector modulator," *Electronic Science & Technology*, Vol. 1, No. 1, 109–112, 2014.
15. Wang, C. and J. Miao, "Implementation and broadband calibration of a multichannel vector modulator module," *IET Sci. Meas. Technol.*, Vol. 11, No. 2, 155–163, 2017.
16. Qiao, H.-L., J.-Y. Yu, and C. Wang, "Study on the real-time phase calibration of interferometer," *Journal of CAEIT*, Vol. 11, No. 4, 574–576, 2016.
17. Kelly, D. F. and W. L. Stutzman, "Array antenna pattern modeling methods that include mutual coupling effects," *IEEE Transactions on Antennas and Propagation*, Vol. 41, No. 12, 1625–1632, 1993.
18. Sayers, A. E., W. M. Dorsey, K. W. O'Haver, et al., "Planar nearfield measurement of digital phased arrays using near-field scan plane reconstruction," *IEEE Transaction on Antennas and Propagation*, Vol. 60, No. 4, 2711–2718, 2012.
19. Medina, R. H., J. L. Salazar, E. J. Knapp, et al., "Calibration and validation of the CASA phased array antenna," *Proceeding of the 42nd European Microwave Conference*, 940–943, Amsterdam, 2012.
20. Mano, S. and T. Katagi, "A method for measuring amplitude and phase of each radiating element of a phased array," *Electronics and Communication in Japan, Part 2*, Vol. 65, No. 3, 58–64, 1982.
21. Haryu, K., I. Chiba, S. Mano, et al., "Near-field measurement method of a phased-array antenna-measurement of element amplitude and phase for array," *Electronics and Communication in Japan, Part 1*, Vol. 79, No. 12, 97–105, 1996.
22. Takahashi, T., Y. Konishi, S. Makino, et al., "Fast measurement technique for phased array calibration," *IEEE Transactions on Antennas and Propagation*, Vol. 56, No. 5, 1888–1899, 2008.
23. Liu, M. and Z. Feng, "Combined rotating-element electric-field vector (CREV) method for nearfield calibration of phased array antenna," *5th International Conference on Microwave and Millimeter Wave Technology*, Guilin, 2007.
24. Matsumoto, Y., I. Yamazaki, and S. Hama, "Calibration method of mutual coupling in beam forming network for phased-array antennas," *Electronics and Communication in Japan, Part 1*, Vol. 84, No. 1, 40–47, 2001.

25. Silverstein, S. D., "Application of orthogonal codes to the calibration of active phased array antennas for communication satellites," *IEEE Transactions on Signal Processing*, Vol. 45, No. 1, 206–218, 1997.
26. Auman, H. M., A. J. Fenn, and F. G. Willwerth, "Phased array antenna calibration and pattern prediction using mutual coupling measurements," *IEEE Transactions on Antennas and Propagation*, Vol. 37, No. 5, 844–850, 1989.
27. Rumiko, Y., K. Yoshihiko, C. Isamu, and K. Takashi, "Beam-shape correction in deployable phased arrays," *IEEE Transactions on Antennas and Propagation*, Vol. 47, No. 1, 482–486, 1999.
28. Toru, T., K. Yoshihiko, M. Shigeru, O. Hiroyuki, and N. Hiromasa, "Fast measurement technique for phased array calibration," *IEEE Transactions on Antennas and Propagation*, Vol. 56, No. 5, 1888–1899, 2008.
29. Analog Devices, Inc., "AD8341 data sheet," 2017, available at http://www.analog.com/media/en-/technical-documentation/data-sheets/AD8341.pdf.
30. Analog Devices, Inc., "AD5668 data sheet," 2017, available at https://www.analog.com/media/en-/technical-documentation/data-sheets/AD5628_5648_5668.pdf.
31. Intel, Inc., "Cyclone III device handbook," 2017, available at https://www.intel.com/content/dam-/www/programmable/us/en/pdfs/literature/hb/cyc3/cyclone3_handbook.pdf.